



HAL
open science

Unprecedented Observations of a Nascent in Situ Cirrus in the Tropical Tropopause Layer

Irene Reinares Martínez, Stéphanie Evan, F G Wienhold, Jérôme Brioude, E. Jensen, T. Thornberry, D. Heron, B Verreyken, S. Körner, H. Vömel, et al.

► **To cite this version:**

Irene Reinares Martínez, Stéphanie Evan, F G Wienhold, Jérôme Brioude, E. Jensen, et al.. Unprecedented Observations of a Nascent in Situ Cirrus in the Tropical Tropopause Layer. *Geophysical Research Letters*, 2021, 48 (4), 10.1029/2020GL090936 . hal-03045631

HAL Id: hal-03045631

<https://hal.science/hal-03045631>

Submitted on 8 Dec 2020

HAL is a multi-disciplinary open access archive for the deposit and dissemination of scientific research documents, whether they are published or not. The documents may come from teaching and research institutions in France or abroad, or from public or private research centers.

L'archive ouverte pluridisciplinaire **HAL**, est destinée au dépôt et à la diffusion de documents scientifiques de niveau recherche, publiés ou non, émanant des établissements d'enseignement et de recherche français ou étrangers, des laboratoires publics ou privés.

Unprecedented Observations of a Nascent in Situ Cirrus in the Tropical Tropopause Layer

I. Reinares Martínez¹, S. Evan¹, F. G. Wienhold², J. Brioude¹, E. J. Jensen³,
T. D. Thornberry^{4,5}, D. Héron¹, B. Verreyken^{1,6,7}, S. Körner⁸, H. Vömel⁹,
J.-M. Metzger¹⁰, F. Posny¹

¹LACy, Laboratoire de l'Atmosphère et des Cyclones, UMR8105, CNRS, Université de La Réunion,

Météo-France, Saint-Denis, La Réunion, France

²Institute for Atmospheric and Climate Science, ETH, Zurich, Switzerland

³National Center for Atmospheric Research, Boulder, Colorado, USA

⁴Chemical Sciences Laboratory, NOAA Earth System Research Laboratory, Boulder, Colorado, USA

⁵Cooperative Institute for Research in Environmental Sciences, University of Colorado Boulder, Boulder,

Colorado, USA

⁶Royal Belgian Institute for Space Aeronomy, Ringlaan 3, 1180 Brussels, Belgium

⁷Department of Chemistry, Ghent University, Krijgslaan 281-S3, 9000 Ghent, Belgium

⁸Deutscher Wetterdienst, Meteorological Observatory Lindenberg, 15848 Lindenberg, Germany

⁹National Center for Atmospheric Research, Boulder, 80301 CO, USA

¹⁰Observatoire des Sciences de l'Univers de La Réunion, UMS3365, CNRS, Université de La Réunion,

Météo-France, Saint-Denis, La Réunion, France

Key Points:

- First in situ observation of a nascent tropical tropopause cirrus
- Homogeneous formation of tiny ice crystals ($<1 \mu\text{m}$) is due to a short vertical scale gravity wave at the tropopause
- Such optically thin cirrus clouds would be missed by current aircraft instruments/remote sensing systems

Abstract

A nascent in situ cirrus was observed on 11 January 2019 in the tropical tropopause layer (TTL) over the southwestern Indian Ocean, with the use of balloon-borne instruments. Data from CFH (Cryogenic Frost Point Hygrometer) and COBALD (Compact Optical Backscatter and Aerosol Detector) instruments were used to characterize the cirrus and its environment. Optical modeling was employed to estimate the cirrus microphysical properties from the COBALD backscatter measurements. Newly-formed ice crystals with radius $<1 \mu\text{m}$ and concentration $\sim 500 \text{ L}^{-1}$ were reported at the tropopause. The relatively low concentration and CFH ice supersaturation (1.5) suggests a homogeneous freezing event stalled by a high-frequency gravity wave. The observed vertical wind speed and temperature anomalies that triggered the cirrus formation were due to a 1.5-km vertical-scale wave, as shown by a spectral analysis. This cirrus observation shortly after nucleation is beyond remote sensing capabilities and presents a type of cirrus never reported before.

Plain Language Summary

Ice clouds are very common in the tropical tropopause layer, a layer of the atmosphere between 14 and 18 km separating the troposphere and the stratosphere. Ice clouds can be formed in situ, generated by cold temperature anomalies due to atmospheric disturbances. In this observational study, we use data from instruments that were flown on the same balloon on 11 January 2019 from Réunion Island, in the southwestern Indian Ocean. We report an ice cloud at the tropopause, at ~ 16.5 km, composed of ice particles with a concentration of more than 500 per liter. This suggests that the ice cloud formed by homogeneous freezing, i.e., the freezing of airborne aqueous solutions. In addition, an abrupt increase in ascent rate of the balloon is related to an atmospheric disturbance which cooled the air and possibly led to the ice cloud formation. The tiny size of the ice crystals indicates that they have just formed. This is a very rare observation because nucleation events are very short.

1 Introduction

In situ cirrus formation in the tropical tropopause layer (TTL, Fueglistaler et al., 2009) occurs as rising air masses reach this extremely cold region (Brewer, 1949; Jensen et al., 1996; Jensen & Pfister, 2004). Cirrus formation and sedimentation contribute to water vapor transport in the TTL, and its entrance value into the low stratosphere, where it has a non-negligible greenhouse effect (Forster & Shine, 2002; Solomon et al., 2010; Dessler et al., 2013). However, the interaction between different-scale dynamical processes driving temperature anomalies in the TTL and the unknown composition of the TTL render the understanding of the cirrus formation very challenging.

Cirrus formation can occur either by homogeneous or heterogeneous ice nucleation mechanisms. For homogeneous freezing of aqueous aerosols, occurring at temperatures below -38°C , theoretical models (e.g., Kärcher & Lohmann, 2002) predict that ice concentrations depend on the cooling rate, rather than on the concentration of aqueous solution droplets, which is rarely a limiting factor. Homogeneous nucleation generally requires conditions of supersaturation above 160% for TTL temperatures (Koop et al., 2000). On the other hand, heterogeneous nucleation depends strongly on the population of ice forming nuclei (IFN, Cziczo et al., 2013; Jensen et al., 2016b), which can be active at much lower supersaturations, but whose abundance is typically limited.

Observations of cirrus in the TTL show that ice concentrations are generally below 100 L^{-1} (e.g., Krämer et al., 2009; Woods et al., 2018). In their recent climatology, Krämer et al. (2020) find median values of ice concentration between 10 and 100 L^{-1} . These values are well below expected numbers for purely homogeneous nucleation. To

74 explain these results, it has been suggested that the main mechanism for low-concentration
75 cirrus formation is heterogeneous nucleation (Cziczo et al., 2013), which is constrained
76 by IFN concentrations. Experimental results reported by DeMott et al. (2003) show median
77 values of heterogeneous IFN concentrations of $\sim 10 \text{ L}^{-1}$ in the free troposphere. Similar
78 measurements have not been made in the TTL, although lower concentrations are
79 expected (Froyd et al., 2009). Several studies have shown, using a box model approach,
80 that low ice concentrations can be generated by homogeneous nucleation if the cooling
81 driving the supersaturation is replaced by warming within the duration of the nucleation
82 event. Such cooling/warming can be attributed to fast changes of phase in high-frequency
83 gravity waves (Jensen et al., 2010; Spichtinger & Krämer, 2013; Dinh et al., 2016). However,
84 Jensen et al. (2016a) argued that the overall impact of the high-frequency waves
85 is to increase ice concentrations produced by homogeneous freezing; the quenching of ice
86 nucleation would only represent 11% of the events. In some infrequent cases, TTL cirrus
87 have been observed with ice concentrations above several thousands per liter (Jensen
88 et al., 2013; Krämer et al., 2020), in which case homogeneous nucleation is the only plausible
89 explanation.

90 High altitude cirrus are common over tropical oceans, and occur with highest frequency
91 over the central and western Pacific, followed by the Indian Ocean (Sassen et al.,
92 2008; Massie et al., 2010). Instrumented aircraft missions from programs like CRAVE
93 (Costa Rica Aura Validation Experiment, e.g., Lawson et al., 2008; Jensen et al., 2008),
94 TWP-ICE (Tropical Warm Pool International Cloud Experiment, e.g., McFarquhar et
95 al., 2007), ATTREX (Airborne Tropical Tropopause Experiment, Jensen et al., 2017),
96 POSIDON (Pacific Oxidants, Sulfur, Ice, Dehydration, and Convection Experiment, Jensen
97 et al., 2018) and StratoClim (Krämer et al., 2020) have provided valuable in situ obser-
98 vations of TTL cirrus, but have been so far mainly restricted to the Pacific Ocean or the
99 Asian monsoon system (in the case of StratoClim). However, little effort has been ded-
100 icated to the undersampled southwestern Indian Ocean, despite the TTL cirrus occur-
101 rence reaching up to 60% during austral summer (Sassen et al., 2008).

102 The aim of this study is to document a singular case of in situ TTL cirrus forma-
103 tion around Réunion Island, in the southwestern Indian Ocean. A set of balloon-borne
104 observations, Lagrangian trajectories and microphysical and optical calculations are pre-
105 sented and used to characterize the microphysical properties and the environment of the
106 observed cirrus. The measurements presented in this study were taken in the framework
107 of the CONCIRTO (CONvection CIRrus tropical Tropopause layer over the indian Ocean)
108 project. This project aims to further our understanding of deep convection and cirrus
109 clouds and how they affect the TTL over the Indian Ocean. It funded coincidental high-
110 resolution balloon-borne in situ measurements of water vapor, ozone and aerosol/ice par-
111 ticles in austral summer 2019 (January-March). In this study, balloon-borne observa-
112 tions of a nascent in situ cirrus encountered on 11 January 2019 are analyzed and the
113 results are interpreted in terms of the different cirrus formation mechanisms.

114 2 Data and Methods

115 2.1 Balloon-borne in situ observations

116 In order to characterize the nascent TTL cirrus cloud and its environment, a COBALD
117 (Compact Optical Backscatter and Aerosol Detector) and CFH (Cryogenic Frost Point
118 Hygrometer) instrument were flown on the same payload on 11 January 2019. Data from
119 the COBALD and CFH were telemetered to the ground by an Internet iMet-1-RSB me-
120 teorological radiosonde, which additionally provided measurements of ambient pressure,
121 temperature and wind speed and direction. The sonde was launched at 17:54 UTC from
122 the Maïdo observatory ($21.1^\circ\text{S}, 55.4^\circ\text{E}$), located on Réunion Island, at 2160 m above sea
123 level.

124 The COBALD backscatter instrument, developed at ETHZ (Swiss Federal Insti-
 125 tute of Technology Zurich), uses two light-emitting diodes at two wavelengths centered
 126 at 455 and 940 nm (blue and infrared, respectively) to detect and characterize cloud and
 127 aerosol particles in the atmosphere (e.g., Brabec et al., 2012; Brunamonti et al., 2018).
 128 The detector has a field of view of $\pm 6^\circ$, and the signal detected typically originates from
 129 a distance of 0.5 to 10 m from the sonde. Beyond 10 m, the signal becomes negligible.

130 For each of the two COBALD wavelengths, the COBALD raw signal is converted
 131 to backscatter ratio (BSR), which is defined as:

$$132 \quad BSR = \frac{\beta_{tot}}{\beta_{mol}} = \frac{\beta_{mol} + \beta_{part}}{\beta_{mol}} = 1 + PBSR \quad (1)$$

133 where $PBSR$ is the particle backscatter ratio; β_{tot} is the measured backscatter coeffi-
 134 cient, expressed as the sum of the molecular (β_{mol}) and particle (β_{part}) contributions.
 135 The particle backscatter coefficient includes aerosols, which are mainly sulfates in the
 136 TTL or lower stratosphere, and ice crystals (β_{ice}). The molecular backscatter coefficient
 137 is computed according to Bucholtz (1995), for stratospheric conditions, corresponding
 138 to 100 hPa and 203 K. The precision of the BSR resulting from the COBALD post-processing
 139 is around 1% in the TTL with an absolute accuracy of better than 5% (Vernier et al.,
 140 2015).

141 The color index (CI) is defined as the ratio of the particle backscatter ratios at the
 142 infrared and blue wavelengths:

$$143 \quad CI = \frac{PBSR_{940}}{PBSR_{455}} \quad (2)$$

144 which is independent of number concentration but depends on the size of the particles.

145 The CFH, developed by Vömel et al. (2007), provides accurate water vapor mea-
 146 surements from the surface to the middle stratosphere. The instrument measures the frost
 147 point temperature, which combined with temperature measurements from the iMet-1-
 148 RSB allows water vapor mixing ratio and supersaturation (S_i) to be calculated using a
 149 saturation vapour pressure formula such as Murphy and Koop (2005) –see their equa-
 150 tion (7)–. CFH water vapor mixing ratio uncertainties are 5% in the tropical troposphere
 151 (Vömel et al., 2007) and 2-3% in the stratosphere (Vömel et al., 2016). At the one per
 152 second telemetry data rate, the CFH and COBALD have a high vertical resolution of
 153 2-3 m with a mean balloon ascent rate of 2-3 m s^{-1} on 11 January 2019. We use the pres-
 154 sure measured by Internet iMet-1-RSB as the main vertical coordinate for all instruments.
 155 All variables are binned in pressure intervals of 1 hPa (corresponding to a vertical res-
 156 olution of ~ 25 m in the TTL) to reduce measurement noise (Brunamonti et al., 2018).

157 2.2 FLEXPART Lagrangian model

158 The origin of air masses sampled at the Maïdo Observatory is assessed using the
 159 FLEXible PARTicle (FLEXPART) Lagrangian Particle Dispersion Model (Stohl et al.,
 160 2005). This transport model is run backward in time and is driven using European Cen-
 161 tre for Medium Range Weather Forecasts - Integrated Forecast System (ECMWF-IFS)
 162 analysis (at 00, 12 UTC) and hourly forecast fields. To compute the FLEXPART tra-
 163 jectories, the ECMWF meteorological fields are retrieved at 0.50° and 0.15° and on full
 164 model levels (137 vertical model levels with a top at 0.01 hPa). Further details on the
 165 model set-up are described in Evan et al. (2020). Here, 100,000 air parcels were distributed
 166 randomly within boxes with a depth of 500 m and $0.10^\circ \times 0.10^\circ$ longitude-latitude bins
 167 centered on the balloon at the cold-point tropopause when the cirrus was observed.

168 2.3 Microphysical and optical modeling

169 To estimate the microphysical properties of the cirrus from the COBALD backscat-
 170 ter ratios, we model the backscatter signal in a similar way as in the Zürich Optical and

171 Microphysical Model (Brabec et al., 2012; Cirisan et al., 2014). A lognormal distribu-
 172 tion of spherical ice crystals population is assumed, following Deshler et al. (2003):

$$173 \quad n(\ln r) = \frac{N_0}{\sqrt{2\pi \ln \sigma}} \exp\left(\frac{-\ln^2\left(\frac{r}{r_M}\right)}{2 \ln^2 \sigma}\right) \quad (3)$$

174 where r_M is the mode radius, σ is the geometric standard deviation parameterizing the
 175 distribution width and N_0 is the total number concentration. This size distribution pos-
 176 sesses three degrees of freedom, r_M , σ and N_0 , thus it cannot be fully constrained by the
 177 two COBALD measurements (BSR_{455} and BSR_{940}). Assuming the crystals sphericity
 178 is a fair approximation under TTL conditions (Woods et al., 2018).

179 The backscatter coefficient from this distribution is evaluated as:

$$180 \quad \beta_{ice} = \int Q_{sc}(x) \pi r^2 n(\ln r) d \ln r \quad (4)$$

181 where $Q_{sc}(x)$ is the efficiency of the backward scattering to the $\pm 6^\circ$ COBALD field of
 182 view for a single ice crystal, depending on the size parameter $x = 2\pi r/\lambda$. It is multiplied
 183 by the ice crystal geometric cross section (πr^2 for a sphere) and summed over the size
 184 distribution.

185 The optical calculus is based on Mie code tabulations to simulate backscatter co-
 186 efficients. For ice particles, the refractive index is set to 1.31. For each wavelength, the
 187 backscatter efficiency Q_{sc} is computed for varying r in intervals of $d \ln r = 0.0023$. Then,
 188 by setting $N_0 = 1 \text{ cm}^{-3}$, equation (4) provides the backscatter coefficient for a size dis-
 189 tribution of one particle per cubic centimeter with a mode radius r_M and width σ . The
 190 $PBSR$ is computed by dividing β_{ice} by the molecular backscatter coefficient, taken again
 191 from Bucholtz (1995). For mode radii below $1 \mu\text{m}$ (in the blue) and below $2 \mu\text{m}$ (in the
 192 infrared), the backscatter coefficient weighted by the distribution (i.e., calculated as in
 193 equation (4) but without the cross section term) is found to linearly track r_M . Up to these
 194 mode radius limits, the $PBSR$ scales with the particle volume, relating it directly to the
 195 ice water content. The ratio of the infrared to the blue $PBSR$ results in the CI , see equa-
 196 tion (2), as function of the mode radius for each size distribution width. Without ad-
 197 ditional constraints on the particle distribution, it is difficult to identify uniquely r_M from
 198 a given CI even for a single σ . This limitation is inherent in the computations of the backscat-
 199 ter coefficients using Mie calculations. With additional constraints, however, provided
 200 by a priori knowledge of the size distributions or microphysical considerations, a mode
 201 radius can be inferred by comparing the measured CI with the simulated CI for a pre-
 202 scribed σ . This finally allows deduction of the ice number concentration and the ice wa-
 203 ter content (IWC) as follows.

204 For each wavelength and prescribed r_M and σ , the total particle number concen-
 205 tration N_0 is found by scaling the ice particle concentration leading to $PBSR = 1$ to
 206 the observed backscatter. That scaling factor is provided by the ratio of molecular backscat-
 207 ter coefficient from Bucholtz (1995) to the result from equation (4) with $N_0 = 1 \text{ cm}^{-3}$
 208 (as mentioned above). With this scaled N_0 the ice water content (IWC) is computed as:

$$209 \quad IWC = \frac{4\pi}{3} r_M^3 N_0 \rho_{ice} \quad (5)$$

210 using $\rho_{ice} = 0.917 \times 10^6 \text{ g m}^{-3}$.

211 3 Results and Discussion

212 3.1 Observed cirrus event

213 The balloon was launched at 17:54 UTC and reached the cold-point temperature
 214 (CPT) of 192.6 K at approximately 16.5 km altitude at 19:40 UTC. The vertical pro-
 215 files of temperature, ascent rate and saturation ratio with respect to ice (S_i) retrieved

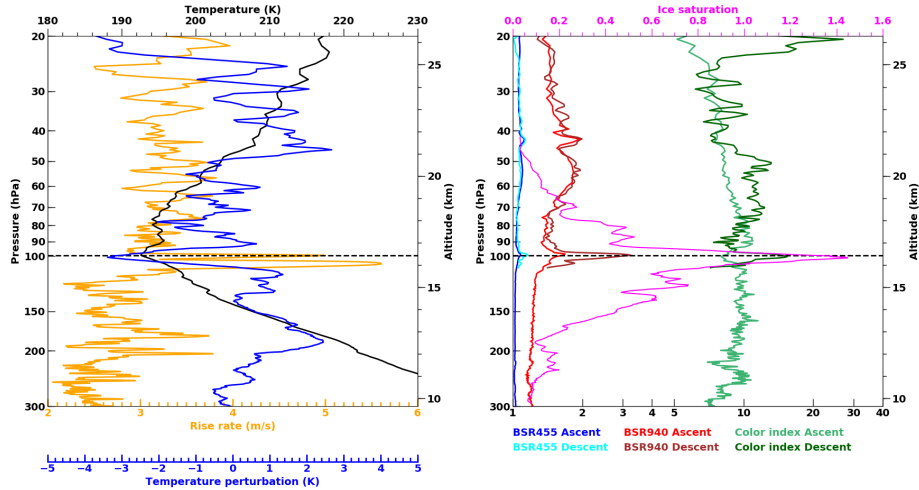


Figure 1. Vertical profiles measured during the sounding at Maïdo observatory on 11 January 2019 at 17:54 UTC. Left: profiles of temperature (black), temperature perturbation (blue) and ascent rate (yellow). Right: profiles of saturation ratio with respect to ice (pink), backscatter ratios at 455 and 940 nm for the ascent (dark blue and red, respectively), and for the descent (cyan and brown, respectively) and color index at ascent/descent (light/dark green). The black dashed line corresponds to the cold point tropopause at ~ 16.5 km altitude.

216 by the iMet and CFH during the ascent of the balloon are shown in Figure 1. During
 217 the descent CFH did not retrieve valuable data. The blue and infrared backscatter ra-
 218 tios measured by the COBALD as well as the associated color index are represented for
 219 both the ascent and descent. At the cold point, peaks in the backscatter ratios are recorded
 220 by COBALD, suggesting the presence of ice crystals. There, the CI (light green curve)
 221 is minimum and has a value of 7.3. This CI signature is roughly 1-km deep and coin-
 222 cides with the BSR maxima. Just below and above the dip, the clear-sky value of the
 223 CI is roughly 10. This background value corresponds to a population of sulfate droplets
 224 on which ice crystals can grow. Concomitant with the backscatter maxima in the ascent,
 225 S_i reaches 1.5. The BSR in the blue and infrared increase at the descent, as well as the
 226 CI , that shows a peak value of 16 (dark green curve).

227 The ascent rate of the balloon is shown on Figure 1. It is calculated following Gallice
 228 et al. (2011) and corresponds to a 60 s-low pass filtered ascent rate profile derived from
 229 the GPS altitude data. The ascent rate is significantly increased by 2 - 3 m s^{-1} between
 230 16 and 16.2 km high, just below the cold point; it is consistent with a gravity wave (GW)
 231 event that would contribute to the observed cooling/supersaturation. A mean temper-
 232 ature profile for January 2019 was computed using 14 radiosonde temperature profiles
 233 measured at the Maïdo Observatory from 7 to 19 January 2019. This allows the com-
 234 putation of the temperature anomaly (Figure 1). The characteristics of the temperature
 235 and vertical speed perturbations, most likely due to a GW event, are analyzed in Sec-
 236 tion 3.4.

3.2 Origin of the sampled air masses

237
 238 Using FLEXPART, a retroplume consisting of 100,000 air parcels is released at 16.5
 239 km altitude and 19:40 UTC, corresponding to the cirrus observation during the ascent.
 240 The trajectories, simulated back to 00 UTC 11 January 2019, are shown on Figure 2.

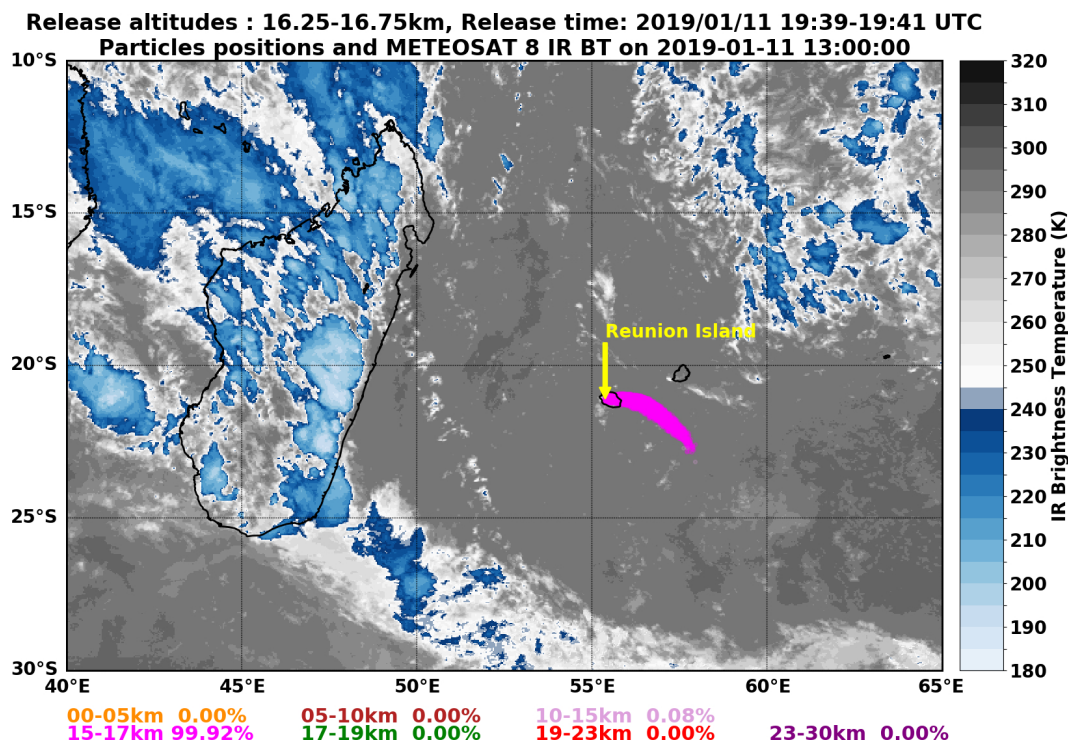


Figure 2. Backward trajectories from the FLEXPART model. They were initialized for the 16.25-16.75 km layer on 11 January 2019, 19:40 UTC around cirrus observation at the ascent of the balloon at the cold-point tropopause. The particle positions (pink dots) and Meteosat8 brightness temperature are shown on 11 January 2019 at 13:00 UTC, meaning that ~ 7 hours before the observation the particles were located in the 15-17 km altitude range.

241 Also displayed on Figure 2 are Meteosat8 brightness temperatures, from a 4-km global
 242 product merging all available geostationary satellites (Janowiak et al., 2001).

243 Almost all the backtrajectories had their origin between 15 and 17 km. The ab-
 244 sence of deep convective clouds along the trajectories further implies that they had not
 245 experienced deep convection, which would be consistent with in situ cirrus formation.
 246 Air masses had been advected from the south-southeast region of Réunion Island with
 247 a high moisture content, according to the ECMWF analyses (not shown). They remained
 248 within the TTL over the southwestern Indian Ocean for the full previous day (not shown).

249 3.3 Microphysical properties of the observed TTL cirrus

250 The *CI* for ice and for the background sulfate aerosols is displayed in Figure 3 as
 251 a function of the mode radius. To simulate the *CI* for ice, three different size distribution
 252 widths are used ($\sigma = 1.3-1.6$) and a refractive index of 1.31. The simulated *CI* for sul-
 253 fate aerosols is shown for a single width ($\sigma = 1.8$) and refractive indexes of 1.45 and 1.51,
 254 which correspond to different H_2SO_4 and H_2O proportions of the aerosols composition.
 255 These values are typical of stratospheric sulfates (Pinnick et al., 1976; Rosen & Kjome,
 256 1991). The radius dependence of the *CI* is remarkably different between ice and sulfate
 257 particles. For ice, the particular dependence on σ and r_M between 0.5 and 2 μm is used
 258 to constrain parameters of the size distribution.

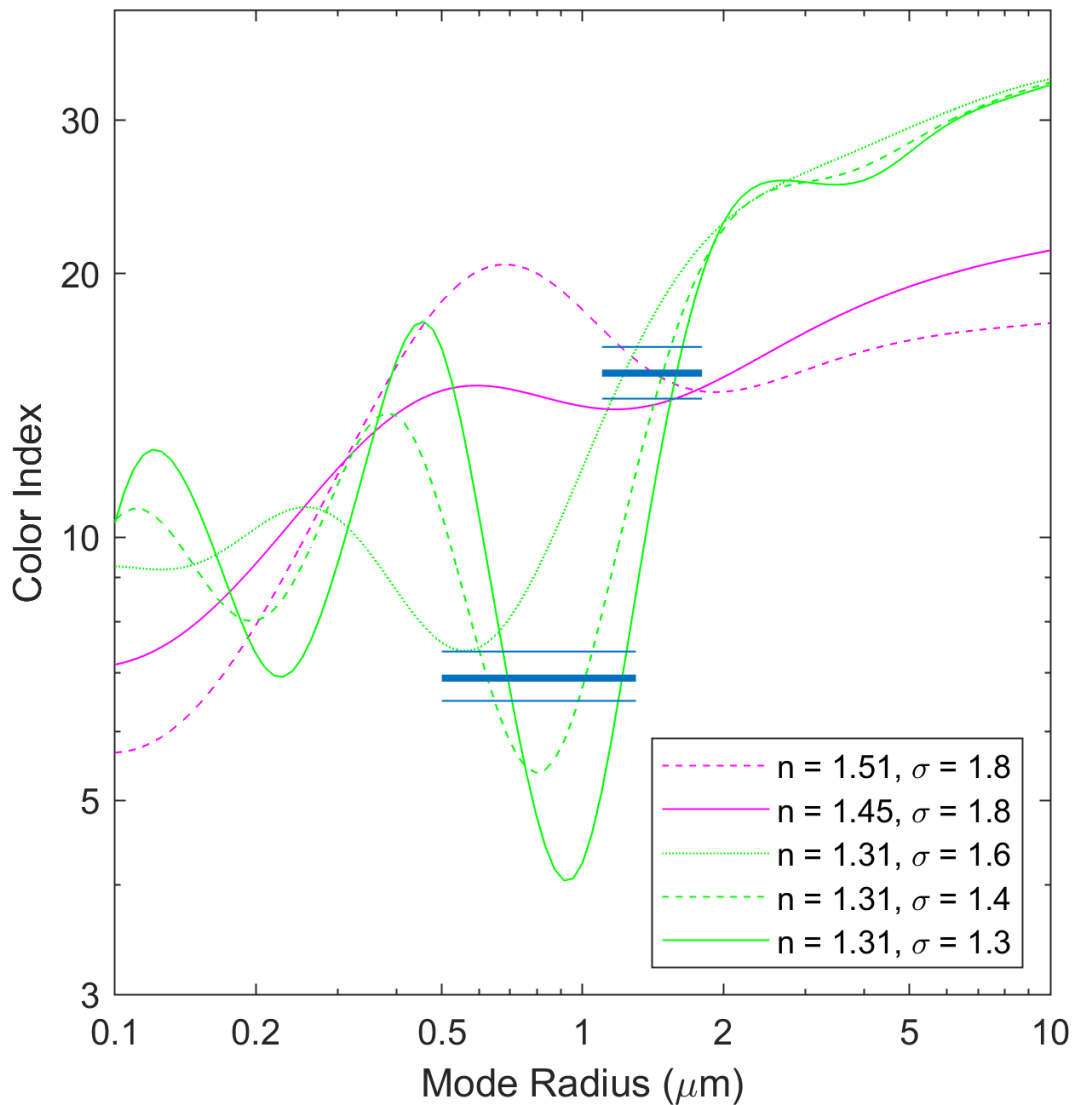


Figure 3. Color index versus mode radius of the ice crystals (green) and sulfate aerosols (pink). For ice, the refractive index (n) is set to 1.31, and three different widths ($\sigma = 1.3, 1.4$ and 1.6) of the lognormal size distribution are used. For the sulfate aerosols, two values of the refractive index ($n = 1.45, 1.51$) are used to simulate the color index for $\sigma = 1.8$. The blue horizontal lines indicate the CI uncertainty range for the ascent (lower lines) and descent (upper lines) observations.

At the ascent, the CI from COBALD measurements was 7.3 (Figure 1). The CI for ice, which is estimated from subtracting the background sulfates signal, is 6.9 and can be as low/high as 6.5/7.4 when accounting for the BSR uncertainty. The observed backscatter cannot be produced with particles smaller than $0.25 \mu\text{m}$ in size. Therefore, the upper CI measurement limit implies σ to be less than 1.8 (the width for the sulfate aerosols) and a mode radius of at least $0.5 \mu\text{m}$. From the observed CI of 16 at the descent, the same analysis yields a CI for ice of 15.4 and a possible range of values from 14.4 to 16.5. These ranges of CI values are shown as blue lines in Figure 3. A single solution for the mode radius does not exist from the obtained values of CI , even when the width of the distribution is prescribed, due to the oscillations of the simulated CI . The dip that manifests for ice slightly above $0.5 \mu\text{m}$ for a width of 1.6 sharpens and moves toward larger size as the distribution width reduces. This change of the mode that constitutes the COBALD signal typically occurs during the initial ice particles growth phase. This unique feature in CI significantly constrains the particle radii. For $\sigma = 1.3\text{--}1.6$ the mode radius can be constrained to $0.5\text{--}1.1 \mu\text{m}$ during ascent and to $1.1\text{--}1.6 \mu\text{m}$ during descent.

The ice number concentration and IWC are deduced from the obtained mode radius for a lognormal distribution with $\sigma = 1.6$. They are estimated to be 520 L^{-1} and $0.43 \mu\text{g m}^{-3}$ during the ascent and 42 L^{-1} and $1.3 \mu\text{g m}^{-3}$ during the descent. The uncertainties of the estimated N_0 and IWC highly depend on the $PBSR$ contribution to the BSR . In this case, the uncertainties range between 10 and 20%. The ice number concentration is reduced by a factor of more than 10 between the ascent and the descent. Heterogeneity of microphysical properties encountered inside cirrus clouds can be explained by small-scale GWs (Jensen et al., 2013). The climatology from Krämer et al. (2020) shows (in their Figure 8) that ice concentrations (for radius above $3 \mu\text{m}$) in young cirrus are most frequently around 100 L^{-1} . Although cirrus with ice concentrations above 10,000 L^{-1} have already been observed (Krämer et al., 2009; Jensen et al., 2009; Krämer et al., 2020), only less than 10% of the observed TTL ice concentrations exceed $1,000 \text{ L}^{-1}$ (Krämer et al., 2020). The estimated IWC values have been previously reported in the same temperature range from in situ retrievals, but lie in the lower edge of the observed range (Krämer et al., 2016; Krämer et al., 2020). During ATTREX 2014 over the western Pacific, direct measurements of IWC were limited to $1 \mu\text{g m}^{-3}$. The cloud probes used could only detect ice crystals with sizes above $1 \mu\text{m}$ (FCDP probe) or $10 \mu\text{m}$ (2D-S probe, Thornberry et al. (2017)). Twenty-seconds average of the FCDP data from ATTREX and POSIDON campaigns allows the sampling of larger volumes of air, leading to IWC below $0.01 \mu\text{g m}^{-3}$. This indicates that while our measurements are sensible, the values found are very rare. The optical depth of the cirrus layer (τ_{cirrus}) is further computed. The uncertainty is much higher in the blue wavelength (90%) compared to the infrared (4–5%), as for the shorter wavelength the molecular Rayleigh scattering is 20 times stronger and the marginal particle scattering on top is much more affected by the observed error. In the infrared, the values of τ_{cirrus} are roughly $1\text{--}2 \times 10^{-4}$ (see supporting information S1 and Figure S1 for details). With these values of the optical depth, the observed cirrus is beyond satellite detection capabilities. For example, for current CALIPSO (Cloud-Aerosol Lidar and Infrared Pathfinder Satellite Observation) V4 sensitivity, the optical depth is barely below 0.003 for night detection (Melody Avery, personal communication).

Analysis of the CI indicate the ice crystals are larger during the descent. Furthermore, the high supersaturation observed by the CFH (1.5) indicates that the environment could support the nucleation and initial growth of ice crystals. A growth calculation is performed to verify the consistency of the ice crystal size change. Neglecting the time dependence of S_i and T , the growth rate of the ice crystals is estimated following Wallace and Hobbs (2006):

$$\frac{dm}{dt} = \frac{4\pi C(S_i - 1)}{f(T)} \quad (6)$$

with

$$f(T) = \left(\frac{L_s}{R_v T} - 1 \right) \frac{L_s}{\kappa T} + \frac{R_v T}{e_i(T) D} \quad (7)$$

where m is the mass of the ice crystal, $\kappa = 2.4 \times 10^{-2} \text{ J m}^{-1} \text{ s}^{-1} \text{ K}^{-1}$ the thermal conductivity of air at 0°C (independent of pressure), $D = 2 \times 10^{-5} \text{ m}^2 \text{ s}^{-1}$ the diffusion coefficient of water vapor in air and $L_s = 2.85 \times 10^6 \text{ J kg}^{-1}$ the gas constant for water vapor. $e_i(T)$ is computed using Murphy and Koop (2005) equation (7).

For a spherical particle, C equals the radius of the crystal. Using $dm/dt = 4\pi\rho_{ice}r^2dr/dt$ with $\rho_{ice} = 0.917 \times 10^6 \text{ g m}^{-3}$ equation (6) yields:

$$r(T) = \sqrt{\frac{2}{\rho_{ice}} \frac{(S_i - 1)}{f(T)} t + r_0^2} \quad (8)$$

where $S_i = 1.5$, $T = 192.6 \text{ K}$, $t = 93 \text{ min}$ and $r_0 = 0.6 \text{ }\mu\text{m}$ (the estimate from COBALD in the ascent). This computation yields a radius of $6 \text{ }\mu\text{m}$. This value is on the same order of magnitude than COBALD estimates for the descent ($1.1\text{-}1.6 \text{ }\mu\text{m}$, see Figure 3). This value is on the same order of magnitude than COBALD estimates for the descent. Moreover, given that the supersaturation was kept constant for the growth rate calculation, the radius of $6 \text{ }\mu\text{m}$ would be an upper limit. The radius obtained from the growth rate calculation is consistent with the hypothesis that the crystals size increased between the COBALD observations at ascent and descent. Given the difference in the two methods used, the agreement in the radius found is reasonable. In reality, the COBALD sampled cirrus regions separated by 88 km (73 km when accounting for the advection). Some matching technique, like the one developed by Cirisan et al. (2014), would be needed to sample the same cirrus twice. Given the ubiquitous small-scale structure in TTL cirrus, it is challenging to relate the cloud properties at two different times and locations.

3.4 Possible mechanisms of cirrus formation

Wavelet analysis using S-transforms (Stockwell et al., 1996) is applied to the temperature anomaly (T') and the ascent rate (w) to deduce the vertical structure of the gravity wave event that most likely triggered the perturbations. This analysis yields a vertical wavelength of 1.5 km for a wave localized near the cold-point tropopause, for both T' and w (see supporting information S2 and Figures S2 to S4 for details on the spectral analysis). The value of 1.5 km agrees with the vertical structure of GWs previously characterized over the tropics with the use of radiosondes. Using 6-hourly radiosonde data, Tsuda et al. (1994) reported GWs with vertical wavelengths ranging from 1 to 4 km in the TTL, with a mean value of 2.5 km . Similarly, using 12-hourly radiosonde data in the equatorial western Pacific, Kim and Alexander (2015) found gravity waves with vertical wavelengths shorter than 2 km (value averaged over a 3-month period, cf. their Figure 5). The amplitude of the perturbations at the cold-point tropopause are estimated to be 1 K and 0.5 m s^{-1} in temperature and vertical speed, respectively. The amplitude of the temperature perturbation is consistent with Kim and Alexander (2013). They found that only 13% of the tropical temperature anomalies due to waves with less than a 3-day period at 17 km altitude had amplitudes larger than 2 K . In addition, Kim and Alexander (2015) determined that those waves with periods between 1 and 3 days accounted for a mean decrease of the CPT of $\sim 0.6 \text{ K}$. Theoretical or box model predictions of ice concentration at comparable temperature generally lead to higher ice concentrations (up to $10,000 \text{ L}^{-1}$) compared to our results ($\sim 500 \text{ L}^{-1}$) for the same vertical wind speed (e.g., Kärcher & Lohmann, 2002; Krämer et al., 2016). For our young cirrus case this difference cannot be explained by sedimentation or the entrainment of surrounding air (which might become important in longer-lived cirrus). Probably, the cirrus observed had not reached the peak ice concentration that would be produced in a persistent updraft because of the truncation of ice nucleation by the phase change of the gravity wave (Jensen et al., 2010; Spichtinger & Krämer, 2013; Dinh et al., 2016).

360 These vertical wind speed and temperature anomalies at the cold-point tropopause
 361 are most likely produced by a convectively generated gravity wave, although different
 362 convective sources could have generated the wave. For example, large-scale organized
 363 convection over Madagascar was very active a few hours before the observation (Figure 2)
 364 and also small-scale oceanic storms developed to the west of Réunion Island during the
 365 evening (not shown). To determine the source of the gravity wave, a full ray-tracing anal-
 366 ysis of the wave is required (e.g., Evan et al., 2012). To perform such an analysis, the
 367 complete spectral characteristics (horizontal/vertical wavelengths, intrinsic frequency)
 368 of the wave would be needed, but this is not possible with a single observation.

369 4 Summary and Conclusion

370 The first observational study of a nascent TTL cirrus over the southwestern Indian
 371 Ocean is presented. On 11 January 2019, a balloon was launched from Réunion Island.
 372 The retrieved data (backscatter ratio from COBALD, water vapor content and super-
 373 saturation from CFH) allow the characterization of the cirrus and environmental forma-
 374 tion conditions. The cirrus is observed at the cold-point tropopause, at ~ 16.5 km alti-
 375 tude. Backtrajectories from the FLEXPART Lagrangian model and the distribution of
 376 deep convection from Meteosat8 show that the air masses sampled by the instruments
 377 at the tropopause had remained over the ocean in the TTL and had not experienced any
 378 convection during the previous day.

379 The color indexes for ice and sulfate aerosols are simulated with an optical model
 380 for a set of lognormal (spherical) particle size distributions. The COBALD measurements
 381 for ice are compared with the simulations to constrain the parameters of the ice crys-
 382 tals distribution. Overall, ice crystal radii are estimated to be smaller than $1 \mu\text{m}$ dur-
 383 ing the ascent. For a radius of $0.6 \mu\text{m}$, the ice water content is $0.43 \mu\text{g m}^{-3}$. The ob-
 384 served supersaturation (1.5) and estimated ice concentration (520 L^{-1}) are consistent
 385 with homogeneous ice formation if the temperature tendency changes during the nucle-
 386 ation event, which can truncate the process and limit the ice concentration (e.g., Spichtinger
 387 & Krämer, 2013; Dinh et al., 2016). Spectral analysis of concomitant observed temper-
 388 ature and vertical wind speed anomalies observed indicates that the nucleation event was
 389 most likely triggered by a gravity wave event of 1 K and 0.5 m s^{-1} amplitudes, respec-
 390 tively. The vertical wavelength is estimated to be 1.5 km for both perturbations. Such
 391 short vertical scale GW event and subsequent cooling/cirrus formation would be diffi-
 392 cult to represent in most current numerical weather prediction and climate models with
 393 coarse vertical resolution in the TTL/lower stratosphere.

394 This study presents unique and rare observations of a relatively low concentration,
 395 very optically thin cirrus ($\tau_{\text{cirrus}} \sim 10^{-4}$). It might result from the quenching of the nu-
 396 cleation event by a high-frequency wave. Such cirrus are difficult to measure remotely
 397 or in situ by current instrumented aircraft. Thus, the occurrence frequency of these thin
 398 cirrus could be greatly underestimated in remote sensing climatologies. This emphasizes
 399 the need for a long-term monitoring system of the TTL composition, with this kind of
 400 CFH-COBALD joint measurements performed here, especially in tropical oceanic regions
 401 with scarce TTL in situ measurements (Müller et al., 2016). Adding an ozone sonde would
 402 also be valuable to better identify air mass origins. To further assess the mechanisms con-
 403 troling this specific cirrus case numerical modeling is needed.

404 Acknowledgments

405 The CONCIRTO project was funded by the Agence Nationale de la Recherche (ANR-
 406 17-CE01-0005-01). We thank OPAR (Observatoire de Physique de l'Atmosphère à La
 407 Réunion, including Maïdo Observatory). It is part of OSU-R (Observatoire des Sciences
 408 de l'Univers à La Réunion), which is funded by Université de la Réunion, CNRS-INSU,

409 Météo-France and the French research infrastructure ACTRIS-France (Aerosols, Clouds
410 and Trace Gases Research Infrastructure).

411 Data from the sounding is available at <https://lacy.univ-reunion.fr/activites/programmes-de-recherche/anr-concirto/donnees>. Meteosat8 data are accessible at https://disc.gsfc.nasa.gov/datasets/GPM_MERGIR_1/summary. The FLEXPART code is available at <https://www.flexpart.eu/> and the ECMWF data can be accessed at <https://apps.ecmwf.int/datasets/>.

415 The authors thank the two anonymous reviewers for their useful comments.

416 References

- 417 Brabec, M., Wienhold, F. G., Luo, B. P., Vömel, H., Immler, F., Steiner, P., ...
418 Peter, T. (2012). Particle backscatter and relative humidity measured across
419 cirrus clouds and comparison with microphysical cirrus modelling. *Atmospheric
420 Chemistry and Physics*, *12*(19), 9135–9148. doi: 10.5194/acp-12-9135-2012
- 421 Brewer, A. (1949). Evidence for a world circulation provided by the measure-
422 ments of helium and water vapour distribution in the stratosphere. *Quar-
423 terly Journal of the Royal Meteorological Society*, *75*(326), 351–363. doi:
424 10.1002/qj.49707532603
- 425 Brunamonti, S., Jorge, T., Oelsner, P., Hanumanthu, S., Singh, B. B., Kumar, K. R.,
426 ... Peter, T. (2018). Balloon-borne measurements of temperature, water
427 vapor, ozone and aerosol backscatter on the southern slopes of the Himalayas
428 during StratoClim 2016–2017. *Atmospheric Chemistry and Physics*, *18*(21),
429 15937–15957. doi: 10.5194/acp-18-15937-2018
- 430 Bucholtz, A. (1995). Rayleigh-scattering calculations for the terrestrial atmosphere.
431 *Applied Optics*, *34*(15), 2765–2773. doi: 10.1364/AO.34.002765
- 432 Cirisan, A., Luo, B., Engel, I., Wienhold, F., Sprenger, M., Krieger, U., ... oth-
433 ers (2014). Balloon-borne match measurements of midlatitude cirrus
434 clouds. *Atmospheric Chemistry and Physics*, *14*(14), 7341–7365. doi:
435 10.5194/acp-14-7341-2014
- 436 Cziczo, D. J., Froyd, K. D., Hoose, C., Jensen, E. J., Diao, M., Zondlo, M. A.,
437 ... Murphy, D. M. (2013). Clarifying the dominant sources and mech-
438 anisms of cirrus cloud formation. *Science*, *340*(6138), 1320–1324. doi:
439 10.1126/science.1234145
- 440 DeMott, P. J., Cziczo, D. J., Prenni, A. J., Murphy, D. M., Kreidenweis, S. M.,
441 Thomson, D. S., ... Rogers, D. C. (2003). Measurements of the concentration
442 and composition of nuclei for cirrus formation. *Proceedings of the National
443 Academy of Sciences*, *100*(25), 14655–14660. doi: 10.1073/pnas.2532677100
- 444 Deshler, T., Hervig, M. E., Hofmann, D. J., Rosen, J. M., & Liley, J. B. (2003).
445 Thirty years of in situ stratospheric aerosol size distribution measurements
446 from Laramie, Wyoming (41°N), using balloon-borne instruments. *Journal of
447 Geophysical Research: Atmospheres*, *108*(D5). doi: 10.1029/2002JD002514
- 448 Dessler, A., Schoeberl, M., Wang, T., Davis, S., & Rosenlof, K. (2013). Stratospheric
449 water vapor feedback. *Proceedings of the National Academy of Sciences*,
450 *110*(45), 18087–18091. doi: 10.1073/pnas.1310344110
- 451 Dinh, T., Podglajen, A., Hertzog, A., Legras, B., & Plougonven, R. (2016). Effect
452 of gravity wave temperature fluctuations on homogeneous ice nucleation in the
453 tropical tropopause layer. *Atmospheric Chemistry and Physics*, *16*(1), 35–46.
454 doi: 10.5194/acp-16-35-2016
- 455 Evan, S., Alexander, M. J., & Dudhia, J. (2012). Model study of intermediate-
456 scale tropical inertia-gravity waves and comparison to TWP-ICE campaign
457 observations. *Journal of the atmospheric sciences*, *69*(2), 591–610. doi:
458 10.1175/JAS-D-11-051.1
- 459 Evan, S., Brioude, J., Rosenlof, K., Davis, S. M., Vömel, H., Héron, D., ... Cam-
460 mas, J.-P. (2020). Effect of deep convection on the tropical tropopause

- 461 layer composition over the southwest Indian Ocean during austral summer.
 462 *Atmospheric Chemistry and Physics*, 20(17), 10565–10586. doi:
 463 10.5194/acp-20-10565-2020
- 464 Forster, P. M. d. F., & Shine, K. P. (2002). Assessing the climate impact of trends
 465 in stratospheric water vapor. *Geophysical Research Letters*, 29(6), 10-1-10-4.
 466 doi: 10.1029/2001GL013909
- 467 Froyd, K. D., Murphy, D. M., Sanford, T. J., Thomson, D. S., Wilson, J. C., Pfister,
 468 L., & Lait, L. (2009). Aerosol composition of the tropical upper tropo-
 469 sphere. *Atmospheric Chemistry and Physics*, 9(13), 4363–4385. doi:
 470 10.5194/acp-9-4363-2009
- 471 Fueglistaler, S., Dessler, A., Dunkerton, T., Folkins, I., Fu, Q., & Mote, P. W.
 472 (2009). Tropical tropopause layer. *Reviews of Geophysics*, 47(1). doi:
 473 10.1029/2008RG000267
- 474 Gallice, A., Wienhold, F. G., Hoyle, C. R., Immler, F., & Peter, T. (2011). Modeling
 475 the ascent of sounding balloons: derivation of the vertical air motion. *Atmo-
 476 spheric Measurement Techniques*, 4(10), 2235–2253. doi: 10.5194/amt-4-2235
 477 -2011
- 478 Janowiak, J. E., Joyce, R. J., & Yarosh, Y. (2001). A real-time global half-hourly
 479 pixel-resolution infrared dataset and its applications. *Bulletin of the American
 480 Meteorological Society*, 82(2), 205-218. doi: 10.1175/1520-0477(2001)082<0205:
 481 ARTGHH>2.3.CO;2
- 482 Jensen, E. J., Diskin, G., Lawson, R. P., Lance, S., Bui, T. P., Hlavka, D., ... Gao,
 483 R. (2013). Ice nucleation and dehydration in the tropical tropopause layer.
 484 *Proceedings of the National Academy of Sciences*, 110(6), 2041–2046. doi:
 485 10.1073/pnas.1217104110
- 486 Jensen, E. J., Kärcher, B., Ueyama, R., Pfister, L., Bui, T. V., Diskin, G. S., ...
 487 others (2018). Heterogeneous ice nucleation in the tropical tropopause
 488 layer. *Journal of Geophysical Research: Atmospheres*, 123(21), 12–210. doi:
 489 10.1029/2018JD028949
- 490 Jensen, E. J., Lawson, P., Baker, B., Pilon, B., Mo, Q., Heymsfield, A. J., ...
 491 Tanelli, S. (2009). On the importance of small ice crystals in tropical
 492 anvil cirrus. *Atmospheric Chemistry and Physics*, 9(15), 5519–5537. doi:
 493 10.5194/acp-9-5519-2009
- 494 Jensen, E. J., & Pfister, L. (2004). Transport and freeze-drying in the tropical
 495 tropopause layer. *Journal of Geophysical Research: Atmospheres*, 109(D2).
 496 doi: 10.1029/2003JD004022
- 497 Jensen, E. J., Pfister, L., Bui, T., Lawson, P., & Baumgardner, D. (2010). Ice
 498 nucleation and cloud microphysical properties in tropical tropopause layer
 499 cirrus. *Atmospheric Chemistry and Physics*, 10(3), 1369–1384. doi:
 500 10.5194/acp-10-1369-2010
- 501 Jensen, E. J., Pfister, L., Bui, T. V., Lawson, P., Baker, B., Mo, Q., ... Smith,
 502 J. A. (2008). Formation of large ($\approx 100 \mu\text{m}$) ice crystals near the tropical
 503 tropopause. *Atmospheric Chemistry and Physics*, 8(6), 1621–1633. doi:
 504 10.5194/acp-8-1621-2008
- 505 Jensen, E. J., Pfister, L., Jordan, D. E., Bui, T. V., Ueyama, R., Singh, H. B., ...
 506 Pfeilsticker, K. (2017, 01). The NASA Airborne Tropical Tropopause Ex-
 507 periment: High-Altitude Aircraft Measurements in the Tropical Western Pa-
 508 cific. *Bulletin of the American Meteorological Society*, 98(1), 129-143. doi:
 509 10.1175/BAMS-D-14-00263.1
- 510 Jensen, E. J., Toon, O. B., Pfister, L., & Selkirk, H. B. (1996). Dehydration of
 511 the upper troposphere and lower stratosphere by subvisible cirrus clouds near
 512 the tropical tropopause. *Geophysical Research Letters*, 23(8), 825–828. doi:
 513 10.1029/96GL00722
- 514 Jensen, E. J., Ueyama, R., Pfister, L., Bui, T. V., Alexander, M. J., Podglajen, A.,
 515 ... others (2016a). High-frequency gravity waves and homogeneous ice nucle-

- 516 ation in tropical tropopause layer cirrus. *Geophysical Research Letters*, *43*(12),
517 6629–6635. doi: 10.1002/2016GL069426
- 518 Jensen, E. J., Ueyama, R., Pfister, L., Bui, T. V., Lawson, R. P., Woods, S., . . .
519 others (2016b). On the susceptibility of cold tropical cirrus to ice nuclei
520 abundance. *Journal of the Atmospheric Sciences*, *73*(6), 2445–2464. doi:
521 10.1175/JAS-D-15-0274.1
- 522 Kärcher, B., & Lohmann, U. (2002). A parameterization of cirrus cloud forma-
523 tion: Homogeneous freezing of supercooled aerosols. *Journal of Geophysical*
524 *Research: Atmospheres*, *107*(D2), AAC–4. doi: 10.1029/2001JD000470
- 525 Kim, J.-E., & Alexander, M. J. (2013). A new wave scheme for trajectory simula-
526 tions of stratospheric water vapor. *Geophysical Research Letters*, *40*(19), 5286-
527 5290. doi: 10.1002/grl.50963
- 528 Kim, J.-E., & Alexander, M. J. (2015). Direct impacts of waves on tropical cold
529 point tropopause temperature. *Geophysical Research Letters*, *42*(5), 1584–
530 1592. doi: 10.1002/2014GL062737
- 531 Koop, T., Luo, B., Tsias, A., & Peter, T. (2000). Water activity as the determinant
532 for homogeneous ice nucleation in aqueous solutions. *Nature*, *406*(6796), 611–
533 614. doi: 10.1038/35020537
- 534 Krämer, M., Rolf, C., Luebke, A., Afchine, A., Spelten, N., Costa, A., . . . oth-
535 ers (2016). A microphysics guide to cirrus clouds – Part 1: Cirrus
536 types. *Atmospheric Chemistry and Physics*, *16*, 3463–3483. doi: 10.5194/
537 acp-16-3463-2016
- 538 Krämer, M., Rolf, C., Spelten, N., Afchine, A., Fahey, D., Jensen, E., . . . Sourdeval,
539 O. (2020). A microphysics guide to cirrus – Part 2: Climatologies of clouds
540 and humidity from observations. *Atmospheric Chemistry and Physics*, *20*(21),
541 12569–12608. doi: 10.5194/acp-20-12569-2020
- 542 Krämer, M., Schiller, C., Afchine, A., Bauer, R., Gensch, I., Mangold, A., . . . others
543 (2009). Ice supersaturations and cirrus cloud crystal numbers. *Atmospheric*
544 *Chemistry and Physics*, *9*(11), 3505–3522. doi: 10.5194/acp-9-3505-2009
- 545 Lawson, R. P., Pilon, B., Baker, B., Mo, Q., Jensen, E., Pfister, L., & Bui, P.
546 (2008). Aircraft measurements of microphysical properties of subvisible cir-
547 rus in the tropical tropopause layer. *Atmospheric Chemistry and Physics*,
548 *8*(6), 1609–1620. doi: 10.5194/acp-8-1609-2008
- 549 Massie, S. T., Gille, J., Craig, C., Khosravi, R., Barnett, J., Read, W., & Winker,
550 D. (2010). HIRDLS and CALIPSO observations of tropical cirrus. *Journal of*
551 *Geophysical Research: Atmospheres*, *115*(D4). doi: 10.1029/2009JD012100
- 552 McFarquhar, G. M., Um, J., Freer, M., Baumgardner, D., Kok, G. L., & Mace, G.
553 (2007). Importance of small ice crystals to cirrus properties: Observations from
554 the tropical warm pool international cloud experiment (TWP-ICE). *Geophys-
555 ical Research Letters*, *34*(13). doi: 10.1029/2007GL029865
- 556 Müller, R., Kunz, A., Hurst, D. F., Rolf, C., Krämer, M., & Riese, M. (2016). The
557 need for accurate long-term measurements of water vapor in the upper tro-
558 posphere and lower stratosphere with global coverage. *Earth’s Future*, *4*(2),
559 25–32. doi: 10.1002/2015EF000321
- 560 Murphy, D. M., & Koop, T. (2005). Review of the vapour pressures of ice and super-
561 cooled water for atmospheric applications. *Quarterly Journal of the Royal Me-
562 teorological Society*, *131*(608), 1539–1565. doi: 10.1256/qj.04.94
- 563 Pinnick, R., Rosen, J., & Hofmann, D. (1976). Stratospheric aerosol measurements
564 III: Optical model calculations. *Journal of the Atmospheric Sciences*, *33*(2),
565 304–314. doi: 10.1175/1520-0469(1976)033<0304:SAMIOM>2.0.CO;2
- 566 Rosen, J. M., & Kjöme, N. T. (1991). Backscattersonde: a new instrument for atmo-
567 spheric aerosol research. *Applied Optics*, *30*(12), 1552–1561. doi: 10.1364/AO
568 .30.001552
- 569 Sassen, K., Wang, Z., & Liu, D. (2008). Global distribution of cirrus clouds from
570 Cloudsat/Cloud-Aerosol Lidar and Infrared Pathfinder Satellite Observations

- 571 (CALIPSO) measurements. *Journal of Geophysical Research: Atmospheres*,
572 *113*(D8). doi: 10.1029/2008JD009972
- 573 Solomon, S., Rosenlof, K. H., Portmann, R. W., Daniel, J. S., Davis, S. M., Sanford,
574 T. J., & Plattner, G.-K. (2010). Contributions of stratospheric water vapor to
575 decadal changes in the rate of global warming. *Science*, *327*(5970), 1219–1223.
576 doi: 10.1126/science.1182488
- 577 Spichtinger, P., & Krämer, M. (2013). Tropical tropopause ice clouds: a dynamic
578 approach to the mystery of low crystal numbers. *Atmospheric Chemistry and*
579 *Physics*, *13*(19), 9801–9818. doi: 10.5194/acp-13-9801-2013
- 580 Stockwell, R. G., Mansinha, L., & Lowe, R. (1996). Localization of the complex
581 spectrum: the S transform. *IEEE transactions on signal processing*, *44*(4),
582 998–1001. doi: 10.1109/78.492555
- 583 Stohl, A., Forster, C., Frank, A., Seibert, P., & Wotawa, G. (2005). Technical note:
584 The lagrangian particle dispersion model FLEXPART version 6.2. *Atmospheric*
585 *Chemistry and Physics*, *5*(9), 2461–2474. doi: 10.5194/acp-5-2461-2005
- 586 Thornberry, T. D., Rollins, A. W., Avery, M. A., Woods, S., Lawson, R. P., Bui,
587 T. V., & Gao, R.-S. (2017). Ice water content-extinction relationships and
588 effective diameter for TTL cirrus derived from in situ measurements during
589 ATTREX 2014. *Journal of Geophysical Research: Atmospheres*, *122*(8), 4494–
590 4507. doi: 10.1002/2016JD025948
- 591 Tsuda, T., Murayama, Y., Wiryosumarto, H., Harijono, S. W. B., & Kato, S. (1994).
592 Radiosonde observations of equatorial atmosphere dynamics over Indonesia: 2.
593 Characteristics of gravity waves. *Journal of Geophysical Research: Atmo-*
594 *spheres*, *99*(D5), 10507–10516. doi: 10.1029/94JD00354
- 595 Vernier, J.-P., Fairlie, T., Natarajan, M., Wienhold, F., Bian, J., Martinsson, B.,
596 ... Bedka, K. (2015). Increase in upper tropospheric and lower strato-
597 spheric aerosol levels and its potential connection with Asian pollution.
598 *Journal of Geophysical Research: Atmospheres*, *120*(4), 1608–1619. doi:
599 10.1002/2014JD022372
- 600 Vömel, H., David, D. E., & Smith, K. (2007). Accuracy of tropospheric and strato-
601 spheric water vapor measurements by the cryogenic frost point hygrometer:
602 Instrumental details and observations. *Journal of Geophysical Research: Atmo-*
603 *spheres*, *112*(D8). doi: 10.1029/2006JD007224
- 604 Vömel, H., Naebert, T., Dirksen, R., & Sommer, M. (2016). An update on the
605 uncertainties of water vapor measurements using cryogenic frost point hy-
606 grometers. *Atmospheric Measurement Techniques*, *9*(8), 3755–3768. doi:
607 10.5194/amt-9-3755-2016
- 608 Wallace, J. M., & Hobbs, P. V. (2006). *Atmospheric science: an introductory survey*
609 (Vol. 92). Elsevier.
- 610 Woods, S., Lawson, R. P., Jensen, E., Bui, T., Thornberry, T., Rollins, A., ... Av-
611 ery, M. (2018). Microphysical properties of tropical tropopause layer cirrus.
612 *Journal of Geophysical Research: Atmospheres*, *123*(11), 6053–6069. doi:
613 10.1029/2017JD028068